Young rotation-powered pulsars as ultraluminous X-ray sources

Aleksei S. Medvedev[1,2] and Juri Poutanen[1]★

[1]*Astronomy Division, Department of Physics, PO Box 3000, FI-90014, University of Oulu, Finland*
[2]*Finnish Centre for Astronomy with ESO (FINCA), University of Turku, Väisäläntie 20, 21500 Piikkiö, Finland*

ABSTRACT

The aim of this paper is to investigate a possible contribution of the rotation-powered pulsars and pulsar wind nebulae to the population of ultraluminous X-ray sources (ULXs). We first develop an analytical model for the evolution of the distribution function of pulsars over the spin period and find both the steady-state and the time-dependent solutions. Using the recent results on the X-ray efficiency dependence on pulsar characteristic age, we then compute the X-ray luminosity function (XLF) of rotation-powered pulsars. In a general case, it has a broken power-law shape with a high-luminosity cutoff, which depends on the distributions of the birth spin period and the magnetic field.

Using the observed XLF of sources in the nearby galaxies and the condition that the pulsar XLF does not exceed that, we find the allowed region for the parameters describing the birth period distribution. We find that the mean pulsar period should be greater than 10–40 ms. These results are consistent with the constraints obtained from the X-ray luminosity of core-collapse supernovae. We estimate that the contribution of the rotation-powered pulsars to the ULX population is at a level exceeding 3 per cent. For a wide birth period distribution, this fraction grows with luminosity and above 10^{40} erg s^{-1} pulsars can dominate the ULX population.

Key words: methods: statistical – stars: luminosity function, mass function – stars: neutron – pulsars: general – X-rays: galaxies.

1 INTRODUCTION

Ultraluminous X-ray sources (ULXs) are non-nuclear, point-like objects with apparent X-ray luminosity exceeding the Eddington limit for a stellar mass black hole (see Feng & Soria 2011, for a review). These objects were discovered by the *Einstein* satellite in nearby star-forming galaxies (Long & van Speybroeck 1983; Fabbiano & Trinchieri 1987; Fabbiano 1988, 1989; Stocke et al. 1991). Observations with *Chandra* and *XMM–Newton* satellites have extended the sample of probable ULXs to about 500 sources (Swartz et al. 2011; Walton et al. 2011).

There are several hypotheses about the nature of ULXs. The most popular models at this moment involve stellar-mass objects similar to SS 433 with the supercritical regime of accretion and mild beaming with a beaming factor $1/b = 4\pi/\Omega \lesssim 10$ (King et al. 2001; Fabrika 2004; Poutanen et al. 2007), or the accreting intermediate mass black holes (IMBH) with masses $M \sim 10^3$–10^5 M$_\odot$ (e.g. Colbert & Mushotzky 1999).

Many ULXs show spectral variability (Kajava & Poutanen 2009) typical for the accreting black holes. The presence of soft thermal excesses sometimes seen in the ULX spectra (Kaaret et al. 2003; Miller et al. 2003) can be used as an argument of a large emission region size, which is either a signature of an IMBH or, alternatively, a large extended photosphere in a strong outflow from stellar-mass objects accreting at super-Eddington rates (Poutanen et al. 2007). The best IMBH candidates, the brightest ULXs, M82 X-1 and ESO 243–49 HLX-1, show spectral states similar to those seen in Galactic sources (Gladstone, Roberts & Done 2009; Feng & Kaaret 2010; Servillat et al. 2011), but at higher luminosities. However, IMBHs cannot dominate the ULX population, because many ULXs are associated with the star-forming regions (Swartz, Tennant & Soria 2009) and young stellar clusters, but are clearly displaced from them by 100–300 pc (Zezas et al. 2002; Kaaret et al. 2004; Ptak et al. 2006; Poutanen et al. 2012). This in turn strongly argues in favour of the young, massive X-ray binaries as the ULX hosts that have been ejected from the stellar clusters by gravitational interactions during cluster formation and/or due to the supernova (SN) explosions. It is very likely, however, that the ULX class is not homogeneous, but contains different kinds of objects.

For example, some of the bright, steady ULXs could be young, luminous rotation-powered pulsars. Earlier studies (Seward & Wang 1988; Becker & Truemper 1997) suggest that the X-ray luminosity of the pulsars is correlated with the rotation energy losses $L = \eta \dot{E}_{\rm rot}$. The efficiency η, which defines the amount of rotational energy losses converted to the X-ray radiation, was found to be nearly constant. Later, using a more complete sample of X-ray rotation-powered pulsars, Possenti et al. (2002) showed that the

★ E-mail: juri.poutanen@oulu.fi

X-ray luminosity depends on the rotational energy loss as a power law $L \propto \dot{E}_{\rm rot}^{1.34}$.

Perna & Stella (2004) performed first Monte Carlo simulations of the X-ray luminosity function (XLF) of rotation-powered pulsars. In order to describe the luminosity evolution of the pulsars together with the evolution of the spin period due to the magnetic-dipole radiation losses, they used the efficiency – characteristic age dependence from Possenti et al. (2002). They considered the distribution functions of pulsars over the magnetic field and the birth spin period given by Arzoumanian, Chernoff & Cordes (2002) and showed that rotation-powered pulsars can be very bright X-ray sources with luminosities $L > 10^{39}$ erg s^{-1}.

Recent investigation of the X-ray properties of rotational-powered pulsars conducted by Vink, Bamba & Yamazaki (2011) revealed a more complicated efficiency–age dependence. Using the new data from *Chandra* observatory (Kargaltsev & Pavlov 2008), they find that radiative efficiency is not constant for pulsars with age $<1.7 \times 10^4$ yr, but depends on the characteristic age. These new results may strongly affect the XLF, increasing the number of the most luminous pulsars.

In this paper, we develop a model for the XLF of the rotation-powered pulsars, taking into account the recently discovered efficiency–age dependence. In Section 2, we present the analytical model describing the evolution of the pulsar periods and find both the steady-state and the time-dependent solutions. Section 3 is devoted to the observational constraints on the model parameters for the birth period and magnetic field distribution that can be obtained from the core-collapsed SNe and the observed XLF of the sources in the nearby galaxies. In Section 4, we obtain the birth period and magnetic field distributions for the brightest pulsars and estimate the possible contribution of young pulsars to the ULX population. We summarize in Section 5.

2 MODEL

2.1 Basic equations

A pulsar is described by two parameters: its birth period p_0 and the magnetic field B, which is assumed to be constant over its lifetime. We consider lognormal distributions for both B and p_0, with the probability density for the decimal logarithm $\log x$ in the following form:

$$G(\log x; \log\langle x\rangle, \sigma_x) = \frac{1}{\sqrt{2\pi}\,\sigma_x} e^{-\frac{\log^2(x/\langle x\rangle)}{2\sigma_x^2}}. \tag{1}$$

The mean and the standard deviation (scale) for the two distributions are $(\log\langle B\rangle, \sigma_B)$ and $(\log\langle p_0\rangle, \sigma_p)$.

The pulsar period at a given age is calculated using a simple model, where the rotational energy losses are dominated by the magnetic dipole radiation (see e.g. Ghosh 2007):

$$\dot{E}_{\rm rot} = -I\Omega\dot{\Omega} = \frac{2R^6}{3c^3}B^2\Omega^4, \tag{2}$$

where $\Omega = 2\pi/p$ is the pulsar rotational frequency, R is the neutron star radius and I is its moment of inertia. We ignore the factor depending on the angle between the dipole and the rotational axis to be consistent with previous studies. The evolution of the pulsar period and the frequency are described by equations

$$p\,\dot{p} = \frac{1}{2}\alpha B^2, \quad \dot{\Omega} = -\frac{\alpha}{8\pi^2}B^2\Omega^3, \tag{3}$$
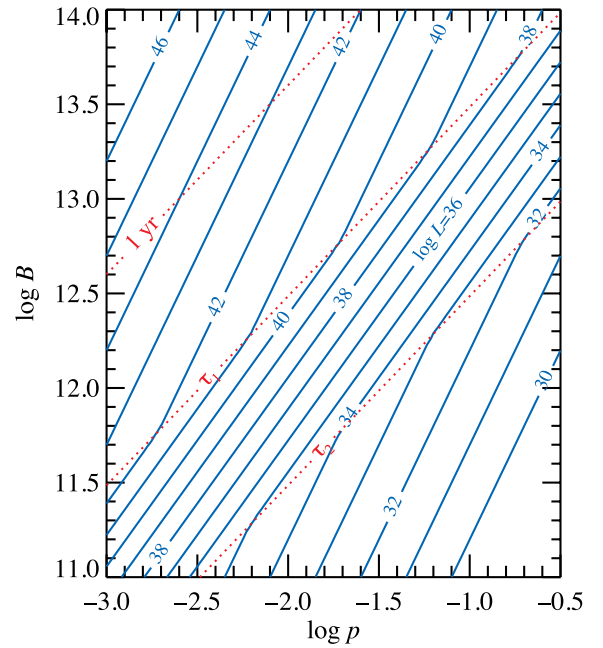

Figure 1. Contour plots of constant X-ray luminosity $\log L$ (solid lines) and the characteristic age τ_c (dotted lines) on the plane magnetic field – period for $\eta_0 = 1$.

where

$$\alpha = \frac{16\pi^2}{3}\frac{R^6}{Ic^3}. \tag{4}$$

The time dependence of the pulsar period is then

$$p(t) = \sqrt{p_0^2 + \alpha B^2 t}, \tag{5}$$

with the characteristic spin-down age

$$\tau_c = \frac{p}{2\dot{p}} = t + \frac{p_0^2}{\alpha B^2} = 5 \times 10^{14} p^2 B_{12}^{-2}\,\text{s}, \tag{6}$$

where we assumed $I_{45} = 1$ and $R_6 = 1$ (i.e. $\alpha \approx 2 \times 10^{-39}$ cgs) and used standard notations $Q = 10^x Q_x$ in cgs units. On the B–p plane, using equation (6) we can identify the lines of constant characteristic age $B_{12} = 3.9\,p_{-3}\,\tau_{c,\rm yr}^{-1/2}$ (see dotted lines in Fig. 1).

We estimate the X-ray luminosity L of a pulsar (and a pulsar wind nebula, PWN) from its period and period derivative following Vink et al. (2011). For simplicity, we approximate the efficiency–age dependence with a simple relation:

$$\eta = L/\dot{E}_{\rm rot} = \begin{cases} \eta_0 & \text{if } \tau_c \leqslant \tau_1, \\ \eta_0\,(\tau_1/\tau_c)^2 & \text{if } \tau_1 \leqslant \tau_c \leqslant \tau_2, \\ 10^{-4} & \text{if } \tau_c \geqslant \tau_2, \end{cases} \tag{7}$$

where $\tau_1 = 170$ yr $\times\ \eta_0^{-1/2}$ and $\tau_2 = 1.7 \times 10^4$ yr. This is equivalent to

$$L = \begin{cases} 4 \times 10^{31} p^{-4} B_{12}^2 \eta_0\ \text{erg s}^{-1} & \text{if } \tau_c \leqslant \tau_1, \\ 4 \times 10^{21} p^{-8} B_{12}^6\ \text{erg s}^{-1} & \text{if } \tau_1 \leqslant \tau_c \leqslant \tau_2, \\ 4 \times 10^{27} p^{-4} B_{12}^2\ \text{erg s}^{-1} & \text{if } \tau_c \geqslant \tau_2. \end{cases} \tag{8}$$

The value of the maximal efficiency η_0 is not well defined because of the lack of young pulsars in the Milky Way. The data seem to indicate that it is at least 0.3 (Kargaltsev & Pavlov 2008; Vink et al. 2011), which we take as a lower limit. In principle, it can even exceed unity, because of the beaming of the pulsar radiation.

In the B–p plane, we can identify the lines of constant luminosity (see solid lines in Fig. 1). Depending on the range of τ_c, these lines have different slopes (see equation 8):

$$B_{12} = \begin{cases} 5 \times 10^{-3} \, p_{-3}^2 L_{39}^{1/2} \eta^{-1/2} & \text{if } \tau_c \leqslant \tau_1 \text{ or } \tau_c \geqslant \tau_2, \\ 0.08 \, p_{-3}^{4/3} L_{39}^{1/6} & \text{if } \tau_1 \leqslant \tau_c \leqslant \tau_2. \end{cases} \tag{9}$$

The line $L = \text{const}$ intersects with the line $\tau_c = \tau_1$ at a point 1 with coordinates $(p_{-3,1}, B_{12,1}) = (60 L_{39}^{-1/2} \eta_0^{3/4}, 18 L_{39}^{-1/2} \eta_0)$, while an intersection with the line $\tau_c = \tau_2$ occurs at point 2 $(p_{-3,2}, B_{12,2}) = (60 L_{33}^{-1/2}, 1.8 L_{33}^{-1/2})$.

As the pulsar period increases, its luminosity drops. If $B_{12} > B_{12,1}$ or $B_{12} < B_{12,2}$, a pulsar crosses the line of a given luminosity being at the constant efficiency branch $\eta = \eta_0$ or $\eta = 10^{-4}$, while for $B_{12,2} < B_{12} < B_{12,1}$ it occurs at the decaying branch of η. Thus, for the fixed magnetic field, the pulsar period at a given luminosity L is

$$p_{-3} = \begin{cases} 14 \, B_{12}^{1/2} L_{39}^{-1/4} \eta_0^{1/4} & \text{if } B_{12} > B_{12,1}, \\ 6.7 \, B_{12}^{3/4} L_{39}^{-1/8} & \text{if } B_{12,2} < B_{12} < B_{12,1}, \\ 45 \, B_{12}^{1/2} L_{33}^{-1/4} & \text{if } B_{12} < B_{12,2}. \end{cases} \tag{10}$$

2.2 Steady-state distributions and the differential luminosity function

2.2.1 Steady-state period distribution

The evolution of the distribution function of pulsars over the period $N(p) = \mathrm{d}N/\mathrm{d}p$ (for a given magnetic field B) can be described by the following evolution equation:

$$\frac{\partial N(p)}{\partial t} = -\frac{\partial}{\partial p}\left[\dot{p}N(p)\right] + Q(p), \tag{11}$$

with the source function describing the production of new pulsars per unit period and time given by

$$Q(p) = \dot{N} \, \frac{1}{p \ln 10} G(\log p; \log\langle p_0\rangle, \sigma_p), \tag{12}$$

and $\dot{N} = \int Q(p)\mathrm{d}p$ is the total production rate per unit time. Equation (11) can be solved analytically and in the steady-state the solution takes the form:

$$N(p) = \frac{1}{\dot{p}} \int_0^p Q(p')\mathrm{d}p'. \tag{13}$$

It reduces to

$$N(p) = \dot{N}\frac{p}{\alpha B^2}\left[1 + \mathrm{erf}\left(\frac{\log(p/\langle p_0\rangle)}{\sigma_p\sqrt{2}}\right)\right], \tag{14}$$

for the source function given by equation (12). At periods which are much larger than the initial periods we obtain

$$N(p) = \frac{\dot{N}}{\dot{p}} = 3.2 \times 10^7 B_{12}^{-2} \, \dot{N}_{\mathrm{yr}} \, p, \tag{15}$$

where $\dot{N}_{\mathrm{yr}}$ is the pulsar birth rate per year.

If the magnetic field and the birth period distributions of the pulsars are lognormal, the steady-state period distribution averaged over the magnetic field distribution is given by

$$\langle N(p)\rangle_B = \dot{N}\frac{e^{2\ln^2 10\,\sigma_B^2}}{\alpha\langle B\rangle^2} p\left[1 + \mathrm{erf}\left(\frac{\log(p/\langle p_0\rangle)}{\sigma_p\sqrt{2}}\right)\right]. \tag{16}$$

For the periods p much larger than $\langle p_0\rangle$, the distribution has a form:

$$\langle N(p)\rangle_B = 3.2 \times 10^7 \, \frac{e^{2\sigma_B^2 \ln^2 10}}{\langle B_{12}\rangle^2} \, \dot{N}_{\mathrm{yr}} \, p, \tag{17}$$

where we used the relation $\langle B^\xi\rangle = \langle B\rangle^\xi \exp\left[(\xi\,\sigma_B\ln 10)^2/2\right]$.

2.2.2 Luminosity distribution

For a given magnetic field, the XLF can be obtained from the period distribution function via transformation

$$L \, N(L) = p \, N(p) \left|\frac{\mathrm{d}\log p}{\mathrm{d}\log L}\right|. \tag{18}$$

For the power-law dependence of luminosity on period $L = C p^{-\gamma}$, we obtain

$$LN(L) = 3.2 \times 10^7 \, B_{12}^{-2} \, \dot{N}_{\mathrm{yr}} \, \frac{1}{\gamma}(L/C)^{-2/\gamma}. \tag{19}$$

For the constant X-ray efficiency η (i.e. $\gamma = 4$), we then easily obtain from equation (8)

$$L \, N(L) = 5 \times 10^3 \, B_{12}^{-1}\eta^{1/2} \dot{N}_{\mathrm{yr}} \, L_{38}^{-1/2}. \tag{20}$$

Thus, for very young, rapidly rotating, luminous pulsars as well as for the old pulsars, the distribution will follow that law (see Fig. 2) In the intermediate regime for $\tau_1 < \tau_c < \tau_2$, $\gamma = 8$ and the XLF follows a shallower dependence:

$$L \, N(L) = 3.2 \times 10^2 \, B_{12}^{-1/2} \dot{N}_{\mathrm{yr}} \, L_{38}^{-1/4}. \tag{21}$$

According to equation (8), the high-luminosity break is expected at $L = 4 \times 10^{41} B_{12}^{-2}$ erg s^{-1}. Smaller mean periods and larger magnetic fields lead to a larger initial luminosity and therefore to a larger number of luminous sources. A corresponding low-luminosity break is at $4 \times 10^{33} B_{12}^{-2}$ erg s^{-1}.

The examples of the XLF normalized to the pulsar birth rate $\dot{N}_{\mathrm{yr}}$ are presented in Fig. 2. The XLF has a complex shape reflecting
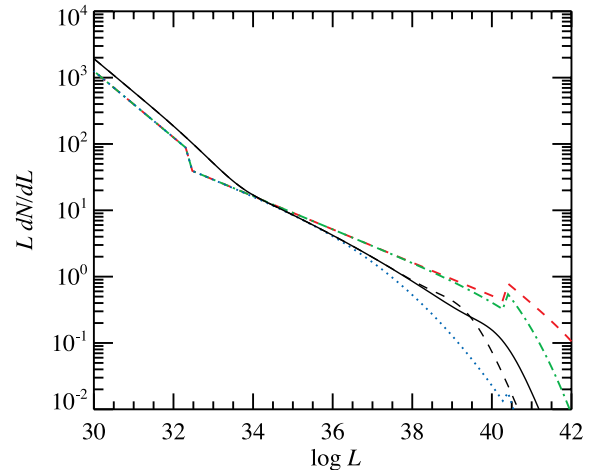

Figure 2. Differential XLF of rotation-powered pulsars for the pulsar birth rate $\dot{N}_{\mathrm{yr}} = 0.01$. The dashed red line shows the XLF for the fixed magnetic field $B_{12} = 4$ and very small birth periods with $\log\langle p_0\rangle = -2.5$ and $\sigma_p = 0.2$. The maximum efficiency is assumed to be $\eta_0 = 1$. The dash–dotted green line corresponds to the larger birth periods with $\log\langle p_0\rangle = -2$, and the XLF for even larger $\log\langle p_0\rangle = -1.5$ is shown by the dotted line. The XLFs averaged over the magnetic field distribution with parameters $\log\langle B\rangle = 12.6$ and $\sigma_B = 0.4$ for the birth period distribution parameters $\log\langle p_0\rangle = -1.7$ and $\sigma_p = 0.2$ are presented by the black solid and dashed lines for the maximum efficiency of $\eta_0 = 1$ and 0.3, respectively.

the behaviour of the X-ray radiative efficiency. The XLF for the fixed B has sharp features reflecting breaks in the derivative of the function $L(p)$ given by equation (8). These breaks are unlikely to be observed, because the actual efficiency–age dependence (7) is likely to be smooth.

The luminosity function of pulsars with the magnetic field distribution $G(\log B; \log \langle B \rangle, \sigma_B)$ can be obtained by averaging the XLFs over that distribution. In this case, the sharp features also disappear (see solid line in Fig. 2). In the range of luminosities corresponding to the constant efficiency, we obtain

$$L N(L) = 5 \times 10^3 \frac{e^{(\sigma_B \ln 10)^2/2}}{\langle B_{12} \rangle} \eta^{1/2} \dot{N}_{\mathrm{yr}} L_{38}^{-1/2}. \tag{22}$$

In the intermediate range of luminosities, the power-law segment has the following form:

$$L N(L) = 3.2 \times 10^2 \frac{e^{(\sigma_B \ln 10)^2/8}}{\langle B_{12} \rangle^{1/2}} \dot{N}_{\mathrm{yr}} L_{38}^{-1/4}. \tag{23}$$

If the birth period distribution has a peak at rather large periods, the XLF has a cutoff before the high-luminosity power-law segment actually starts (e.g. see black solid line in Fig. 2). Decreasing the maximum efficiency η_0 leads to a smaller cutoff luminosity (compare solid and dashed black curves in Fig. 2), while the intermediate power law barely changes.

Radiation from a pulsar may be confined within a narrow beam ~ 1 str (Tauris & Manchester 1998) corresponding to the beaming factor $b = \Omega/4\pi = 0.1$. However, young pulsars have PWN, which are more isotropic. The ratio of the observed luminosities of the nebula to the pulsar has a large spread, but typically is of the order of unity (Kargaltsev & Pavlov 2008). This argues against strong beaming and therefore we take $b > 0.3$. The normalization of the observed luminosity function scales linearly with the beaming factor.

2.3 Non-stationary solution

2.3.1 Evolution of the period distribution

In order to determine the distribution of pulsars over the period at a given pulsar age, we need to solve the time-dependent evolution equation (11):

$$\frac{\partial N(p,t)}{\partial t} + \frac{\partial}{\partial p}[\dot{p} N(p,t)] = 0, \tag{24}$$

with the following initial condition at zero age:

$$N(p, t=0) = N_0(p). \tag{25}$$

According to equation (5), the period derivative can be expressed as $\dot{p} = \alpha B^2/2p$. Equation (24) conserves the total number of pulsars N. Its solution is

$$N(p,t) = p \frac{N_0(p_0)}{p_0}, \tag{26}$$

where $p_0 = \sqrt{p^2 - \alpha t B^2}$. The solution is only defined for

$$p \geqslant B\sqrt{\alpha t}. \tag{27}$$

Function $N(p, t)$ has the mean

$$\langle p \rangle(t) = \int_0^\infty p \, N(p,t) \, \mathrm{d}p = \int_0^\infty \sqrt{p_0^2 + \alpha t B^2} \, N_0(p_0) \mathrm{d}p_0, \tag{28}$$

and the variance

$$\sigma_p^2(t) = \int_0^\infty (p - \langle p \rangle)^2 \, N(p,t) \, \mathrm{d}p$$

$$= \int_0^\infty \left(\sqrt{p_0^2 + \alpha t B^2} - \langle p \rangle \right)^2 N_0(p_0) \, \mathrm{d}p_0. \tag{29}$$

At large ages, the mean becomes

$$\langle p \rangle(t) \approx \sqrt{\alpha t} B + \frac{\langle p_0^2 \rangle}{2\sqrt{\alpha t} B}, \tag{30}$$

and the variance is

$$\sigma_p^2(t) \approx \frac{\langle p_0^4 \rangle - \langle p_0^2 \rangle^2}{4\alpha t B^2} \to 0. \tag{31}$$

Thus, the solution becomes the delta function:

$$N(p, t \to \infty) = N \, \delta(p - \sqrt{\alpha t} B). \tag{32}$$

This can be easily understood from equation (5), which describes the evolution of the pulsar period with time. At large age, the time-dependent term becomes much greater than the value of the initial spin period. Thus, every pulsar with a given magnetic field at a given age has the same period $p(t) = \sqrt{\alpha t} B$. Therefore, at large ages the period distribution of the pulsars does not contain any information about the initial one. The characteristic time-scale at which the information about the initial distribution is lost can be estimated as:

$$t \approx \frac{1}{\alpha} \left(\frac{p_0}{B} \right)^2 \approx 1600 \left(\frac{p_{0,-2}}{B_{12}} \right)^2 \, \mathrm{yr}, \tag{33}$$

where $p_{0,-2}$ is the birth period expressed in 10 ms.

We can now obtain the solution averaged over the magnetic field distribution

$$\langle N(p,t) \rangle_B = \int_{-\infty}^\infty N(p,t) \, G(\log B; \log \langle B \rangle, \sigma_B) \, \mathrm{d}\log B. \tag{34}$$

It is useful to introduce dimensionless variables

$$\rho = \frac{p}{\langle p_0 \rangle}, \quad \beta = \frac{B}{\langle B \rangle}, \quad \tau = \alpha \left(\frac{\langle B \rangle}{\langle p_0 \rangle} \right)^2 t, \tag{35}$$

and find the solution as a function of dimensionless period ρ and time τ, such as $\langle N(\rho, \tau) \rangle_B = \langle N(p,t) \rangle_B \times \langle p_0 \rangle$ and $\int \langle N(\rho, \tau) \rangle_B \mathrm{d}\rho = N$. For the lognormal distribution of both magnetic field and birth periods, we obtain

$$\langle N(\rho, \tau) \rangle_B = N \frac{\rho}{2\pi\sigma_p\sigma_B \ln^2 10}$$

$$\times \int_0^{\rho/\sqrt{\tau}} \frac{\mathrm{d}\beta}{\beta(\rho^2 - \tau\beta^2)} \exp \left\{ -\frac{\log^2 \sqrt{\rho^2 - \tau\beta^2}}{2\sigma_p^2} - \frac{\log^2 \beta}{2\sigma_B^2} \right\}. \tag{36}$$

An asymptote at large τ can be easy obtained directly substituting equation (32) to (34):

$$\langle N(\rho, \tau \to \infty) \rangle_B = \frac{N}{\rho \ln 10} G(\log \rho; \log \sqrt{\tau}, \sigma_B). \tag{37}$$

This implies that the mean of the distribution $\rho N(\rho)$ increases with time as $\langle \rho \rangle = \sqrt{\tau}$ and the dispersion is completely determined by the width of the magnetic field distribution σ_B. The evolution of the period distribution is presented in Fig. 3. If $\sigma_p < \sigma_B$, then at large τ, the period distribution is wider than the initial one, while in the opposite case, $\sigma_p > \sigma_B$, the period distribution becomes narrower.
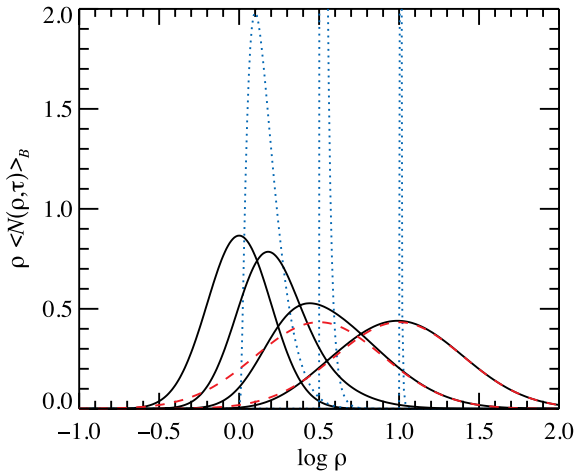
Figure 3. Evolution of the (normalized) period distribution with time. The black solid lines show the evolution of period distribution with initial $\sigma_p = 0.2$ averaged over magnetic field distribution with $\sigma_B = 0.4$ for $\tau = 0, 1, 10, 100$ (from left to right). The blue dotted line shows the period distribution for a specific magnetic field ($\beta = 1$) at $\tau = 1, 10$ and 100. The distribution becomes very narrow at large τ, peaking at $\rho = \sqrt{\tau}$. The red dashed lines represent the asymptotic solution (37) at large τ, which just reflects the lognormal distribution of the magnetic field.

2.3.2 Evolution of the luminosity distribution

In order to obtain the luminosity distribution, we take the time-dependent solution for the period distribution (26), use the transformation (18) and average the derived expression over the magnetic field. Resulting distribution and its evolution is presented in Figs 4 and 5, respectively. As it is clearly seen from Fig. 4, the initial luminosity distribution of the pulsars can be multimodal. Every mode of the distribution is related to the different regime of the luminosity–period dependence. Also, the luminosity distribution at birth may reveal the narrow spikes, related to the breaks in the $dp(L)/dL$ derivative. The luminosity distribution is broader for larger σ_p and σ_B. The distribution becomes narrower and more symmetric as the time increases (Fig. 5). This happens because at birth, pulsars can
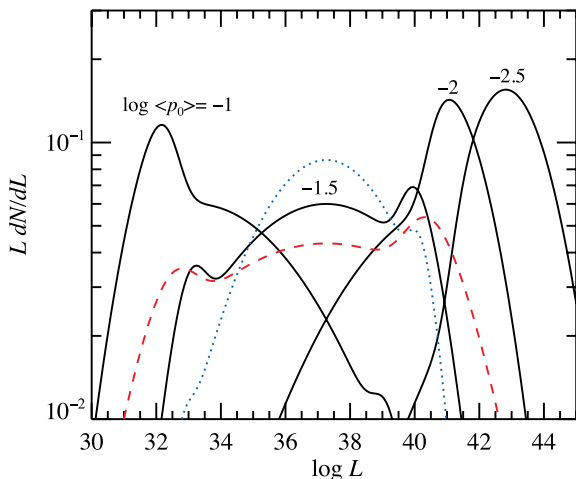

Figure 4. Normalized luminosity distribution at birth for different values of birth period with $\sigma_p = 0.2$, $\log \langle B \rangle = 12.6$, $\sigma_B = 0.4$ and $\eta_0 = 1$ (black lines). The blue dotted and red dashed lines show the luminosity distribution with $\sigma_B = 0.2$ and $\sigma_p = 0.4$, respectively, for $\log \langle p_0 \rangle = -1.5$ (other parameters are the same).
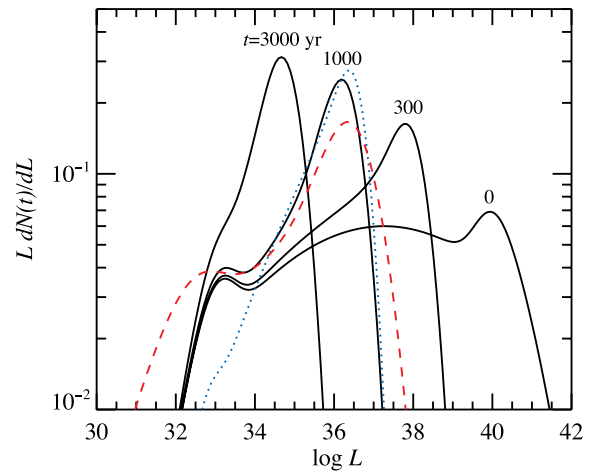

Figure 5. Evolution of the pulsar normalized luminosity distribution for the initial distribution with the following parameters $\log \langle p_0 \rangle = -1.5$, $\sigma_p = 0.2$, $\log \langle B \rangle = 12.6$, $\sigma_B = 0.4$ and $\eta_0 = 1$ (black solid lines). The blue dotted and red dashed lines shows the luminosity distribution at 1000 yr for $\sigma_B = 0.2$ and $\sigma_p = 0.4$, respectively (other parameters are the same). The luminosity distribution becomes more symmetric at large age.

operate in the different regimes of conversion of the rotational energy losses to the X-ray radiation, depending on the spin period and the magnetic field distributions. With time, all pulsars move towards the same regime, where the efficiency is constant $\sim 10^{-4}$ (see equation 7).

3 OBSERVATIONAL CONSTRAINTS ON MODEL PARAMETERS

3.1 Previous determination of magnetic field and birth period distributions

Distributions of the pulsars over the magnetic field and the birth period were investigated in several papers based on the analysis of the observed radio (Arzoumanian et al. 2002; Faucher-Giguère & Kaspi 2006) and the gamma-ray pulsars (Gonthier et al. 2002; Takata, Wang & Cheng 2011). Parameters of the magnetic field distribution are similar in all these studies lying in the range $\log \langle B \rangle = 12.35$–$12.75$, $\sigma_B = 0.1$–0.55 (see Table 1). However, parameters of the birth period distributions are significantly different: the mean logarithm $\log \langle p_0 \rangle$ varies from -2.3 to -0.5 (i.e. periods in the range from 5 to 200 ms) and the width σ_p varies in the range 0–0.8 (see Table 1; the parameters were estimated by fitting the lognormal distribution to the actual distributions adopted by the authors). This difference in the birth period distributions is most likely caused by a low sensitivity of the considered models to the birth period. As it was shown on Section 2, the period distribution of the pulsars at large time does not contain information about the birth periods. Therefore, in order to determine these parameters we have to use only young pulsars.

Recently, Popov & Turolla (2012) have presented new estimates of the birth periods based on a sample of radio pulsars associated with the SN remnants. They showed that the distribution has to be rather wide, and it is consistent with a Gaussian with the mean $p_0 \sim 0.1$ s and width $\sigma \sim 0.1$ s. However, this result is inconclusive, because the number of objects in the used sample is not large enough to derive the exact shape of the period distribution.

The analysis of the observed luminosity distribution of the historical core-collapse SNe by Perna et al. (2008) showed that the

Table 1. Birth rates and parameters of the magnetic field and the birth period distributions for rotation-powered pulsars.

Model	$\log \langle p_0 \rangle$	σ_p	$\log \langle B \rangle$	σ_B	$\dot{N}_{yr}$[a]	Reference[b]
1	−2.3	0.3[c]	12.35	0.4	0.0013	1
2	−1.52	0.0	12.75[d]	0.33[d]	0.01[e]	2
3	−0.52[f]	0.8[f]	12.65	0.55	0.028[g]	3
4	−1.7[h]	0.1[h]	12.6	0.1	0.01	4

[a]Birth rate of pulsars in the Milky Way per year.
[b]References: (1) Arzoumanian et al. (2002); (2) Gonthier et al. (2002); (3) Faucher-Giguère & Kaspi (2006); (4) Takata et al. (2011).
[c]Reference 1 gives the lower limit on σ_p of 0.2. Taking a broader distribution with $\sigma_p > 0.3$ does not affect the results.
[d]Parameters for the lognormal distribution were estimated by fitting a more complex distribution adopted in Reference 2, see their table 1 and equation 1.
[e]Value from the first line of Table 8 of Reference 2.
[f]Parameters for the lognormal distribution were estimated by fitting a Gaussian distribution adopted in Reference 3, see their table 8.
[g]Birth rate from table 8 of Reference 3.
[h]The lognormal distribution approximates the flat distribution in the 20–30 ms range adopted in Reference 4.

predicted number of bright pulsars in the Perna & Stella (2004) model is much larger than the observed number of luminous SNe. This discrepancy is related to the assumed very short (5 ms) mean birth period from Arzoumanian et al. (2002). On the other hand, using parameters of the pulsar magnetic field distribution from Faucher-Giguère & Kaspi (2006), Perna et al. (2008) found that in order to satisfy the observed luminosity distribution of the historical core-collapse SNe, the birth period of the pulsars should be larger than 40–50 ms.

In the following sections, we repeat the analysis by Perna et al. (2008) using a different efficiency–age dependence given by equation (7) as well as using the new data that became available after 2008. We also obtain constraints on the pulsar birth period distribution by comparing the simulated pulsar XLF with the observed XLF of the bright sources in the nearby galaxies derived by Mineo, Gilfanov & Sunyaev (2012).

3.2 Constraints from the luminosity distribution of core-collapse SNe

Perna et al. (2008) proposed that constraints on the birth period distribution can be obtained by comparing the observed luminosity distribution of historical core-collapse SNe with the simulated pulsar XLF (for the given ages), considering that the most probable remnant of the core-collapse SN explosion is a neutron star.

One of the important questions is the earliest age at which SNe can be used to derive the observational luminosity distribution that would reflect the XLF of the brightest rotation-powered pulsars. There are two main issues here. The first problem is the high optical depth of the SNR shell at the earliest stages of its expansion. According to Chevalier & Fransson (1994), the optical depth of SNR changes with time as

$$\tau \sim \frac{5}{t_{yr}^2}, \tag{38}$$

for typical parameters of the SN explosion (kinetic energy $E_0 \sim 10^{51}$ erg, mass of the ejecta $M_{ej} \sim 10 \, M_\odot$, and typical photon energy $E \sim 10$ keV). Therefore, the SNR shell becomes optically thin in about three years. However, Perna et al. (2008) limited their SNe subsamples by the minimal age of 10 and 30 yr. As a

result, they did not include the most luminous SNe in their analysis. Furthermore, because of the finite size and rapid expansion of the shell, the diffusion time of photons in the SNR shell can be small enough to make the X-ray radiation of the central pulsar visible at even earlier times. Considering that the number of scatterings in the SNR shell of optical depth $\tau \gg 1$ scales as $N \sim \tau^2$, we can estimate the escape time of the photons from the shell:

$$t_D(t) \sim \frac{\tau(t) R_{SNR}(t)}{c}, \tag{39}$$

where $R_{SNR}(t)$ is the size of SNR. Because of the free expansion stage for SNe with ages $\lesssim 100$ yr, the size of SNR will increase with time as

$$R_{SNR}(t) = \sqrt{\frac{2E_0}{M_{ej}}} t. \tag{40}$$

Therefore, the diffusion time is

$$t_D \approx \frac{0.05}{t_{yr}} \text{ yr.} \tag{41}$$

The diffusion time is equal to the age of SN at $t \sim 0.2$ yr and later it is always smaller. Therefore, a significant fraction of the SNR radiation may be produced by the central pulsar, because the luminosity of a typical newborn pulsar may achieve 10^{40}–10^{41} erg s^{-1}, which is comparable to the highest observed SNe luminosities in our sample.

The second issue is the fallback accretion on to a neutron star during early phases of SN explosion. According to Chevalier (1989), radiation from the central pulsar begins to diffuse through the accreting matter when a reverse shock radius reaches the radiation trapping radius. It happens at $\gtrsim 0.5$ yr after the SN. Therefore, we can expect that the central pulsars will contribute to the total luminosity after 0.5–1.0 yr. This estimate is close to the limit coming from the diffusion time arguments. Thus, we will use the minimal age $t = 0.5$ yr.

Another important question is a selection effect, which may strongly affect the observed luminosity distribution of SNe, because the younger is the source the brighter it is and the higher is the probability for it to be detected. For example, most of the SNe luminosity measurements from Perna et al. (2008) are upper limits, because those sources are quite faint. Only 19 brightest and youngest sources have actual measurements of luminosity. Compilation of Dwarkadas & Gruszko (2012) contains additional 11 sources with known luminosity, but there are only four sources with ages >0.5 yr. In addition, because some fraction of the SNe X-ray luminosity is not related to the pulsar or PWN, also the actual X-ray detections here should be treated as upper limits on the pulsar luminosity. For the analysis, we use the data on the ages and the X-ray luminosities of core-collapse SNe (with ages >0.5 yr) from Perna et al. (2008) with the addition of the new measurements from the compilation of Dwarkadas & Gruszko (2012) (see Tables 2 and 3). The cumulative histogram of upper limits is shown in Fig. 6 by the bold pink line.

We follow the recipe described in Section 2.3.2 and calculate the luminosity distribution of 76 pulsars for the ages of SNe listed in Tables 2 and 3. We then construct the average normalized cumulative distribution of luminosities $f(<L)$ and compare it to the observed distribution. In the absence of beaming (i.e. $b = 1$), from Fig. 6(a), we see that only model 3 (Faucher-Giguère & Kaspi 2006) satisfies the upper limit distribution, for the maximum efficiency η_0 between 0.3 and 1. Model 2 (Gonthier et al. 2002) is also reasonably close, especially for $\eta_0 = 0.3$.

Table 2. X-ray luminosities of historical SNe.

SN	Age (yr)[a]	log L	References[b]
1979C	26.8	$38.43^{+0.06}_{-0.07}$	1
1986E	19.6	$38.15^{+0.13}_{-0.19}$	1
1986J	21.2	$38.93^{+0.02}_{-0.03}$	1
1988Z	15.5	$39.46^{+0.07}_{-0.08}$	1
1990U	10.9	$39.04^{+0.19}_{-0.26}$	1
1994I	8.2	$36.90^{+0.02}_{-0.04}$	1
1995N	8.9	$39.63^{+0.09}_{-0.11}$	1
1996cr	4.2	$39.28^{+0.08}_{-0.10}$	1
1998S	3.6	$39.58^{+0.05}_{-0.06}$	1
1998bw	3.5	$38.60^{+0.10}_{-0.11}$	1
1999ec	5.9	$39.49^{+0.05}_{-0.06}$	1
2001em	4.7	$40.76^{+0.08}_{-0.10}$	1
2001gd	1.1	$39.00^{+0.11}_{-0.15}$	1
2001ig	0.5	$37.54^{+0.20}_{-0.37}$	1
2004C	3.1	$38.00^{+0.11}_{-0.10}$	1
2005ip	1.3	$40.20^{+0.07}_{-0.09}$	2
2005kd	1.2	$41.41^{+0.06}_{-0.07}$	1
2006jd	1.1	$41.40^{+0.12}_{-0.17}$	3,4
2008ij	0.56	$39.00^{+0.11}_{-0.15}$	5

[a] Ages of SNe were calculated from the detection times listed at the website of the IAU Central Bureau for Astronomical Telegrams, except for SNe from Perna et al. (2008).
[b] References: (1) Perna et al. (2008); (2) Immler & Pooley (2007); (3) Immler et al. (2007); (4) Dwarkadas & Gruszko (2012); (5) Immler et al. (2009).

Table 3. Upper limits for the X-ray luminosities of historical SNe (from Perna et al. 2008).

SN	Age (yr)	log L
1923A	77.3	35.78
1926A	75.3	37.15
1937A	67.3	37.11
1937F	62.1	36.43
1940A	63.0	37.00
1940B	62.6	36.93
1941A	60.2	36.74
1948B	55.1	35.67
1954A	48.9	35.20
1959D	41.6	37.34
1961V	38.3	37.79
1962L	41.2	37.67
1962M	40.3	35.57
1965H	37.7	38.18
1965L	37.8	36.76
1968L	32.0	36.18
1969B	32.6	36.58
1969L	30.3	37.68
1970G	33.9	36.69
1972Q	30.5	38.48
1972R	31.9	35.86
1973R	25.9	37.89
1976B	26.2	37.95
1980K	24.0	36.81
1982F	22.6	36.04
1983E	19.0	37.66
1983I	17.8	36.23
1983N	16.8	36.74
1983V	19.1	37.85
1985L	14.9	37.91
1986I	17.1	38.48
1986L	18.9	38.15
1987B	14.1	38.18
1988A	12.3	37.38
1991N	11.8	37.62
1993J	8.1	38.00
1994ak	7.4	37.57
1996ae	5.9	37.79
1996bu	6.6	37.32
1997X	6.1	37.34
1997bs	2.5	38.46
1998T	5.2	38.30
1999dn	4.4	37.77
1999el	5.6	38.75
1999em	1.0	37.15
2000P	7.2	39.08
2000bg	1.3	39.15
2001ci	2.5	37.70
2001du	1.3	37.58
2002ap	0.9	36.49
2002fjn	4.7	39.11
2002hf	3.1	38.88
2003dh	0.7	40.70
2005N	0.5	40.00
2005at	1.7	38.48
2005bf	0.6	39.78
2005gl	1.6	39.53

An additional effect appears if beaming is significant. Then most of the pulsars which appear to be faint in the X-rays, in reality could be very bright sources, but beamed away from us. Furthermore, about 10 per cent of SNe produce a black hole after explosion instead of a neutron star (Heger et al. 2003), which can be modelled as an additional multiplicative beaming factor 0.9. The cumulative normalized luminosity function in that case would start from the value $1 - 0.9b$ at the low-luminosity end. For example, for a smaller beaming factor $b = 0.3$, most of the bright pulsars would be undetected. In that case, models 2 and 3 satisfy the upper limit distributions, model 4 is only marginally consistent with them, but model 1 (Arzoumanian et al. 2002) still contradicts the data.

We can also find more general constraints on the parameter set $(\log \langle p_0 \rangle, \sigma_p)$. With some high probability, the cumulative model distribution should be above the observed histogram of upper limits $f(< L)$ at any luminosity. We can formalize this condition by computing the fraction of model distributions that satisfy the constraint

$$\min_L \left\{ \frac{f_{\text{pulsars}}(< L)(\langle \log p_0 \rangle, \sigma_p)}{f_{\text{SNe}}(< L)} \right\} > 1. \quad (42)$$

Using Monte Carlo method, we simulate 3000 sets of 76 pulsars at given ages (see Tables 2 and 3) which follow given magnetic field and the initial period distributions, accounting for beaming and for the 10 per cent black hole fraction. We then find the dependence $\sigma_p(\langle p_0 \rangle)$, which satisfies condition (42) in 90 and 68 per cent cases. The results depend on b and η_0 (see Fig. 6b). The mean birth period of the pulsars cannot be shorter than $\sim$15–30 ms for any σ_p. For larger dispersion $\sigma_p \sim 1$, the limiting value is between 60 ms and 1 s, depending on the parameters and the

sought probability. The constraints depend much stronger on beaming than the assumed maximal efficiency η_0, because they come mostly from the low-luminosity SNe, whose number is not affected much by variation of η_0. Our constraints on the mean periods are
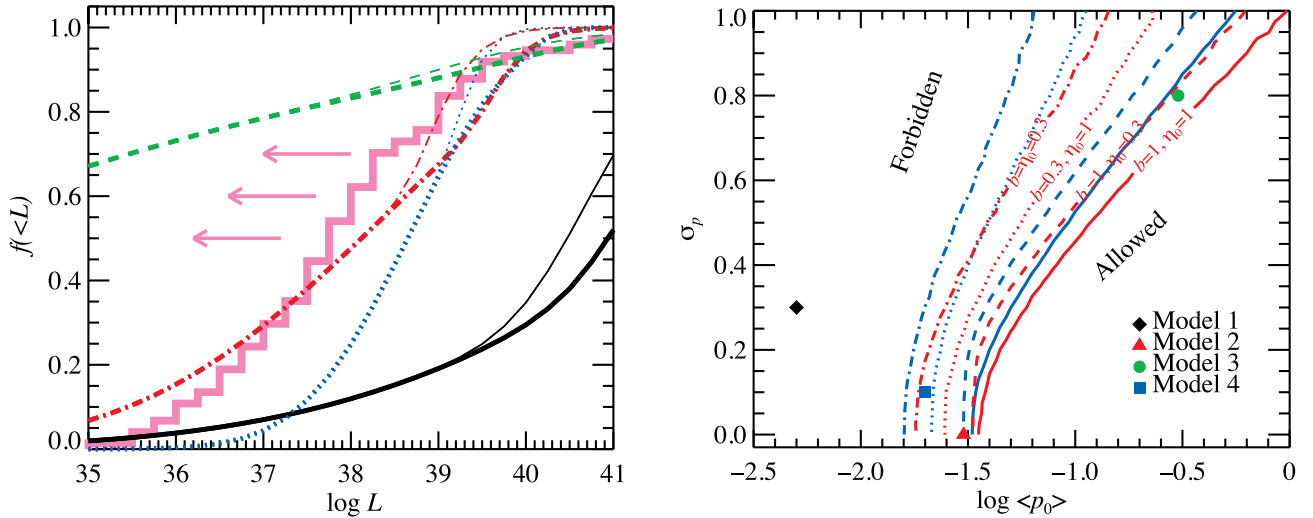
Figure 6. (a) Cumulative normalized luminosity distributions for SNe (either measurements or upper limits; pink histogram) with ages $t > 0.5$ yr. The black solid, red dash–dotted, green dashed and blue dotted lines correspond to average distributions for models 1–4 from Table 1, respectively. Thick lines are for the case $\eta_0 = 1$ and the thin lines are for $\eta_0 = 0.3$. Here, no beaming is assumed ($b = 1$). (b) Allowed region for the parameters of the birth period distribution. Parameters along the red and blue lines satisfy condition (42) in 90 and 68 per cent cases, respectively. The solid, dashed, dotted and dot–dashed lines correspond to different pairs of $(b, \eta_0) = (1,1)$, $(1,0.3)$, $(0.3,1)$ and $(0.3,0.3)$, respectively. Regions to the right of these lines satisfy the data with higher probability. The calculations are performed for the average values of the magnetic field distribution $\log \langle B \rangle = 12.6$ and $\sigma_B = 0.4$. The positions of parameters listed in Table 1 are marked by different symbols.

consistent with those derived by Perna et al. (2008), who found $\langle p_0 \rangle > 40$–50 ms.

3.3 Constraints from the XLF for sources in nearby galaxies

3.3.1 Averaged XLF of nearby galaxies

The averaged XLF of the bright sources in nearby star-forming galaxies was recently obtained by Mineo et al. (2012). The star formation rates (SFRs) in the galaxies of their sample are spread in a broad interval between ~ 0.1 and $\sim 100 \, M_\odot \, yr^{-1}$. The observed XLF is well approximated by a power law:

$$\frac{dN}{dL_{38}} = 1.88 \times L_{38}^{-1.59} \times SFR[M_\odot \, yr^{-1}]. \tag{43}$$

Mineo et al. (2012) introduce the cutoff at $L_{\mathrm{cut}, 38} = 10^3$, because of lack of statistics at luminosities above $10^{41} \, erg \, s^{-1}$. Here, we do not introduce the cutoff and integrate the relation (43) to infinity to derive the cumulative distribution:

$$N(> L_{38}) = 3.2 \times L_{38}^{-0.59} \times SFR. \tag{44}$$

3.3.2 Comparisons of the pulsar and observed XLF

In order to make the comparisons between the pulsar XLF and the observed XLF of sources in the nearby galaxies, we first need to find the relation between the pulsar birth rate and the SFR. We assume the Galactic $SFR_{MW} = 2 \, M_\odot \, yr^{-1}$, in accordance with the recent study of Chomiuk & Povich (2011). However, using luminous radio SN remnants and the X-ray point sources, these authors found that the Milky Way deviates from SFR expectations at the 1–3σ level, hinting that the Galactic SFR is overestimated or extragalactic SFRs need to be revised upward.

The estimations for the birth rate of pulsars in the Milky Way differs by an order of magnitude in various papers (see Table 1),

and on average is about 0.02 yr^{-1}. The conversion between pulsar birth rate and the SFR can be expressed as follows:

$$\dot{N} \left[yr^{-1} \right] = \kappa \times SFR \left[M_\odot \, yr^{-1} \right], \tag{45}$$

with the conversion factor κ varying between 0.0007 (in model 1) and 0.014 (in model 3), with the mean of about 0.01.

Using the conversion formula (45), we can now produce the cumulative luminosity distribution of pulsars normalized by the SFR and compare it to the observed XLF from Mineo et al. (2012). The XLFs calculated for the four models from Table 1 are presented in Fig. 7a. We see that all cumulative XLF are harder than the observed XLF at luminosities below $10^{38} \, erg \, s^{-1}$. This fact is easy to understand from our Fig. 2 and equation (21): the typical slope of 1.25 is related to the intermediate characteristic ages (see equation 7), where the efficiency varies strongly. The position of the cutoff depends not only on the mean birth period, but also on the width of the distribution. For example, model 3 has the largest mean period, but because of a large dispersion, the XLF extends to very high luminosities without a visible break. On the other hand, model 2 has a rather small mean period, but the XLF cuts off sharply, because of the zero σ_p and the absence of fast pulsars. Model 1 has the largest number of bright pulsars because of the smallest mean period (see also Fig. 2). Model 4 also shows a cutoff at rather small luminosity in spite of the small initial periods, because of the narrow magnetic field distribution.

The number of high-luminosity pulsars depends on the maximum efficiency η_0. Decreasing η_0 leads to a smaller cutoff luminosity (compare thick and thin curves in Fig. 7a). However, if the cutoff is at very large luminosity (as e.g. in the case of models 1 and 3), variations in η_0 do not affect significantly the observed XLF, at least in the range of luminosities $\log L < 40$. The XLF normalization scales linearly with the beaming factor b.

Dividing the pulsar cumulative XLF by the observed XLF, we obtain the fraction of pulsars as a function of luminosity. It is an increasing function of luminosity and reaches the maximum
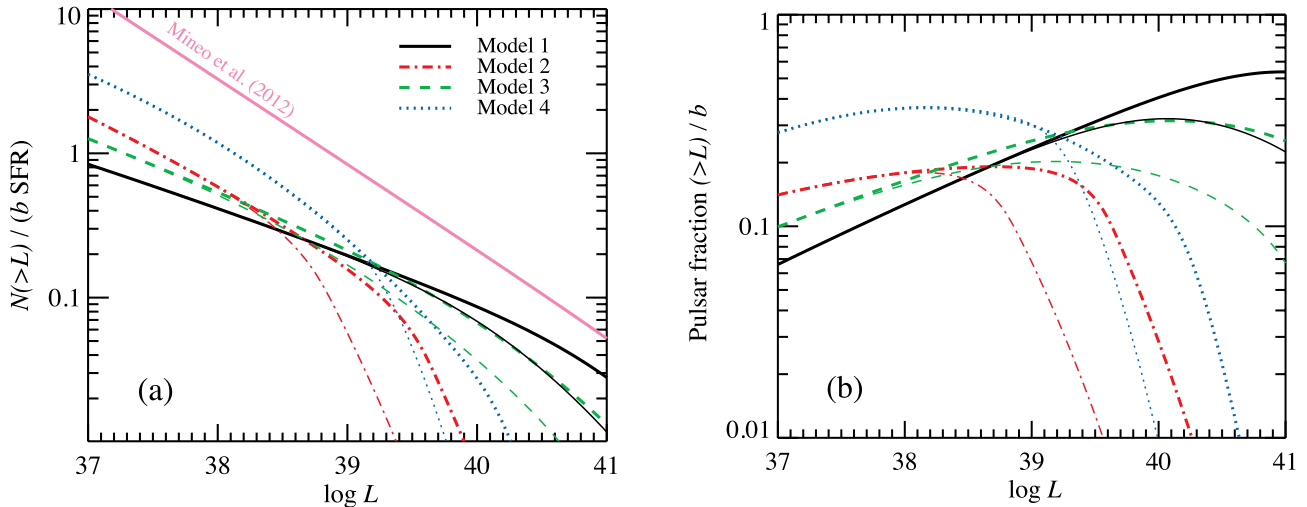
Figure 7. (a) Cumulative luminosity distribution of the pulsars normalized to the unit SFR and unit beaming $b = 1$. The black solid, red dash–dotted, green dashed and blue dotted lines correspond to models 1–4, respectively. The thick and thin lines correspond to the maximum efficiency of $\eta_0 = 1$ and 0.3, respectively. The pink solid straight line represents the average cumulative XLF of sources in the nearby galaxies (Mineo et al. 2012) taken in the form (44). (b) The predicted fraction (above a given luminosity) of pulsars in the high-luminosity end of the average XLF. Each line corresponds to the same models as in panel (a).

at $\log L$ between 38 and 41, depending on the model parameters, see Fig. 7(b). The maximum pulsar fraction reaches $(0.2$–$0.5)b$ for all models.

3.3.3 Constraints on the birth period distribution

The differential XLF of the pulsars should not exceed the observed XLF at any luminosity. This condition gives us the opportunity to find constraints on the birth period distribution. We can find the dependence $\sigma_p(\langle p_0 \rangle)$, which satisfies the condition

$$\max_{L < L_{\max}} \left\{ \frac{\mathrm{XLF}_{\mathrm{pulsars}}(L, \langle \log p_0 \rangle, \sigma_p)}{\mathrm{XLF}_{\mathrm{Mineo}}(L)} \right\} = 1, \tag{46}$$

where $L_{\max} = 10^{41} \mathrm{\,erg\,s^{-1}}$ corresponds to the maximal luminosity considered by Mineo et al. (2012). As with the constraints from the SNe, here the results depend on the assumed values of η_0 and b (see Fig. 8). As we see, the mean birth period (for $b = 1$ and $\eta_0 = 1$) has to be larger than 25–250 ms, depending on the width of the period distribution. Parameters considered by Arzoumanian et al. (2002) and Takata et al. (2011) lie in the forbidden region. Parameters from other papers listed in Table 1 are in the allowed region. However, as it was shown by Popov & Turolla (2012), the period distribution has to be rather wide and to cover the range of periods from tenths to hundreds of milliseconds. Only the distribution found by Faucher-Giguère & Kaspi (2006) satisfies this condition.

For a smaller value of the maximal efficiency $\eta_0 = 0.3$, the critical line (red bold dashed line in Fig. 8) shifts to the left and depends weaker on σ_p. Thus, the decrease of the efficiency leads to shorter allowed periods. Variations in the beaming factor lead to a stronger effect. For $b = 0.3$ and $\eta_0 = 1$, the allowed region extends beyond the parameters from Takata et al. (2011), but still cannot reach the parameters from Arzoumanian et al. (2002).

We note here that for simulations we used the average value of the pulsar birth rate $\kappa = 0.01$, while it is more than 10 and two times smaller in models of Arzoumanian et al. (2002) and Takata et al. (2011), respectively. Thus, all considered models are in principle allowed if one corrects for different κ. However, for small b and η_0 the constraints coming from the SNe (see Fig. 6b) are actually

stronger and rule out model 1, with model 4 being only marginally consistent with the data.

4 PULSAR CONTRIBUTION TO ULX

4.1 Dependence on the birth period distribution

The total number of the luminous pulsars with luminosities greater that $10^{39} \mathrm{\,erg\,s^{-1}}$ is very similar in all four models 1–4 (see Fig. 7a):

$$N_{\mathrm{obs}}(\log L > 39) \approx 0.3 \times b \times \mathrm{SFR} \,[\mathrm{M_\odot\,yr^{-1}}]. \tag{47}$$

At larger luminosities this number depends strongly on the period distribution and the maximum efficiency. For example, model 2 predicts less than $0.01b \times \mathrm{SFR}$ pulsars above $10^{40} \mathrm{\,erg\,s^{-1}}$ because of the cutoff at $\sim 2 \times 10^{39} \mathrm{\,erg\,s^{-1}}$ in the XLF (see Fig. 7a). On the other hand, model 3 gives about $0.08b \times \mathrm{SFR}$ very bright pulsars. The pulsar fraction in the observed XLF at $\log L > 39$ can be as high as $(0.2$–$0.3)b$ for all models. At even higher luminosities, this fraction drops in models 2 and 4 and increases in models 1 and 4.

We can also calculate the pulsar fraction dependence on the combination $(\log \langle p_0 \rangle, \sigma_p)$. This fraction calculated for sources with luminosities $\log L > 39$ and >40 is presented as contours in Fig. 8. We see that the models 2 and 3 lie nearly on the same curve. The explicit dependence of the pulsar fraction on the parameters of the birth period distribution is shown in Fig. 9. We see that for small initial mean periods, the pulsar fraction is nearly independent of σ_p because the XLF cuts off at very high luminosities. The situation changes dramatically at large $\langle p_0 \rangle$: the narrow period distribution now predicts cutoff at low luminosity and the pulsar fraction is negligible. At large widths $\sigma_p \sim 1$, the pulsar fraction is still large because of the large extent of the XLF. Situation is similar for the cutoff luminosity $\log L = 40$, but now for small σ_p the XLF cuts off close to the limiting luminosity even for rather short initial periods and the pulsar fraction is small in that case. For large $\sigma_p \sim 1$, the pulsar fraction exceeds that fraction for $\log L = 39$ if $\log \langle p_0 \rangle \lesssim -0.5$.
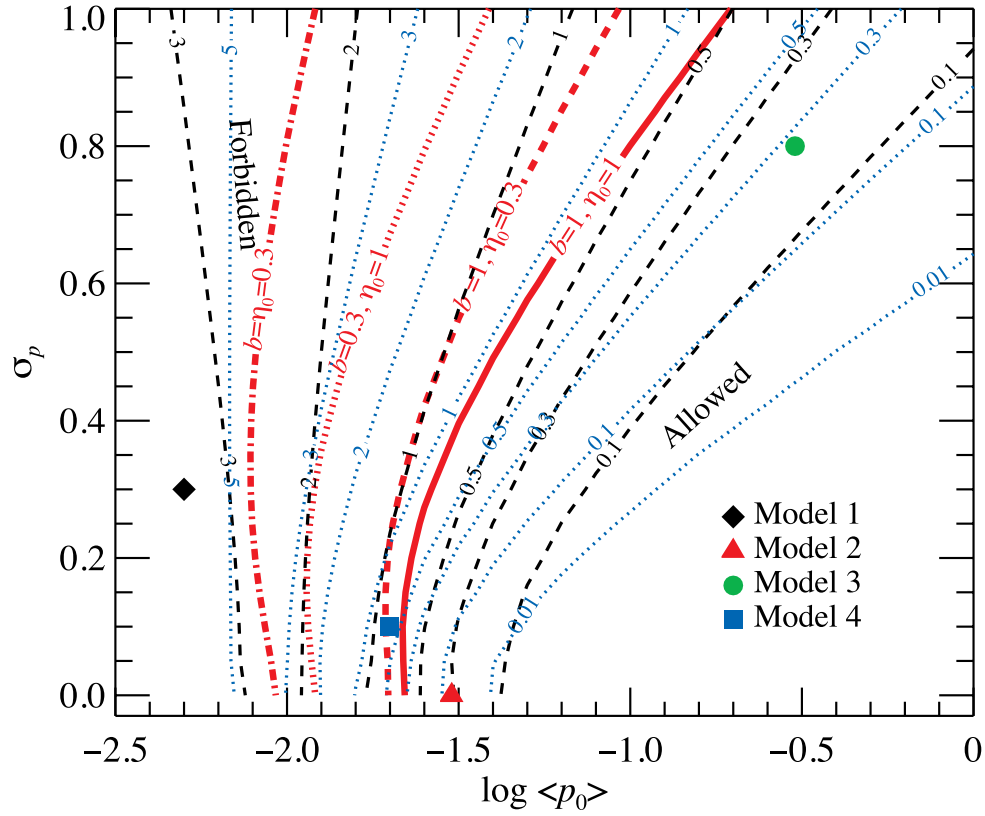
Figure 8. Allowed region for the parameters of the birth period distribution derived from the XLF of sources in the nearby galaxies and the fraction of pulsars in the observed cumulative XLF (Mineo et al. 2012). Parameters along the bold red lines satisfy equation (46). The solid, dashed, dotted and dot–dashed lines correspond to different pairs of $(b, \eta_0) = (1,1)$, $(1,0.3)$, $(0.3,1)$ and $(0.3,0.3)$, respectively. The regions to the right of these lines are allowed and to the left are forbidden. The dashed black and dotted blue contours give the pulsar fraction for $b = 1$ at luminosities above 10^{39} and 10^{40} erg s^{-1}, respectively. Calculations are performed for the average values $\log \langle B \rangle = 12.6$, $\sigma_B = 0.4$ and $\kappa = 0.01$. The positions of parameters listed in Table 1 are marked by different symbols.
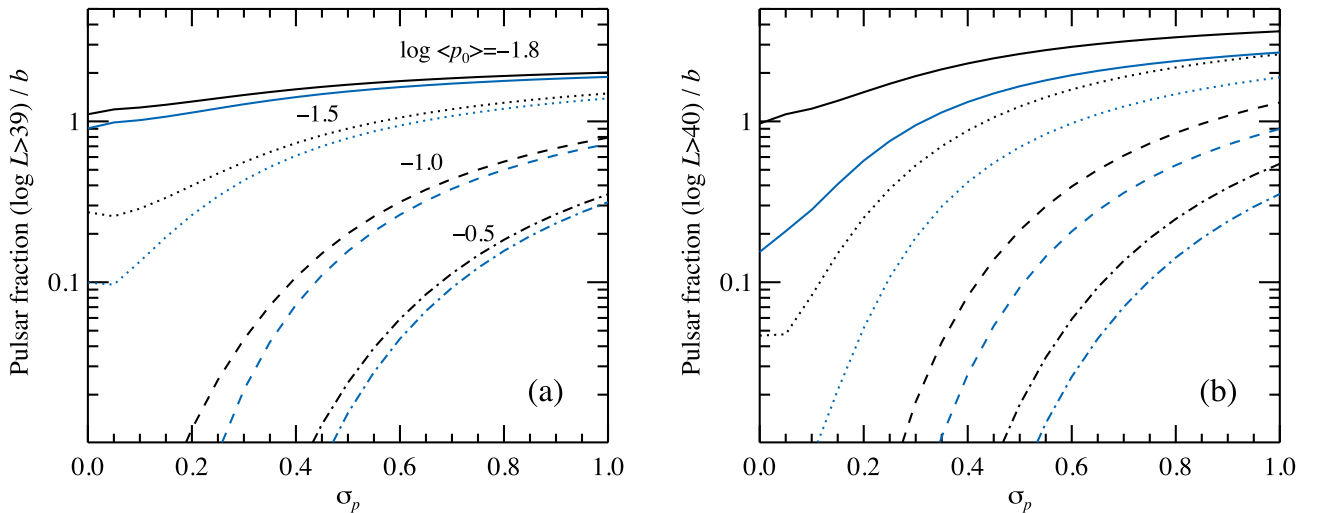

Figure 9. The fraction of the pulsars in the observed cumulative XLF (Mineo et al. 2012) at luminosities above 10^{39} erg s^{-1} (panel a) and above 10^{40} erg s^{-1} (panel b) (see Section 4.1) as a function of σ_p. The solid, dotted, dashed and dot–dashed lines correspond to the mean period of $\log \langle p_0 \rangle = -1.8$, -1.5, -1.0 and 0.5, respectively. The upper black and the lower blue lines give the pulsar fraction for $\eta_0 = 1$ and 0.3, respectively. Calculations are performed for the values $\log \langle B \rangle = 12.6$, $\sigma_B = 0.4$ and $\kappa = 0.01$.

4.2 Dependence on the maximum efficiency

In a general case, the dependence of the pulsar fraction above $\log L = 39$ on η_0 can be easily seen in Fig. 9a. For small initial periods, the pulsar fraction is nearly independent of η_0 for all σ_p

because the XLF extends to very high luminosities. For larger initial mean periods, the dependence on η_0 is strong for narrow distributions $\sigma_p \sim 0$, because the XLF has a sharp cutoff around $\log L = 39$. For broad initial distributions with $\sigma_p \sim 1$, the pulsar fraction is still rather large and the dependence on η_0 is not so strong.
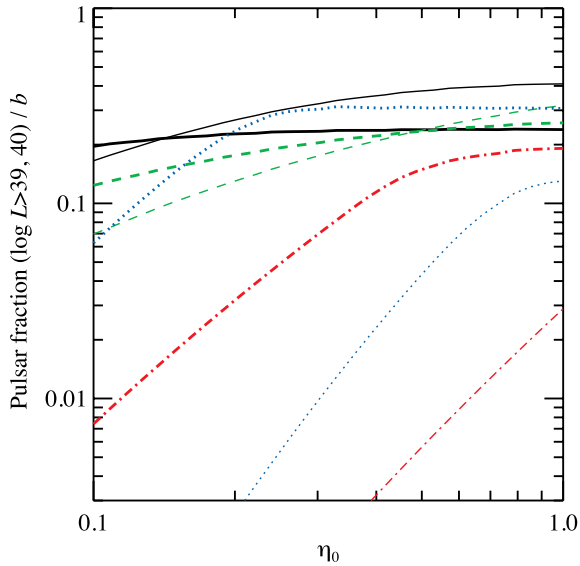
Figure 10. The predicted fraction of pulsars at luminosities above 10^{39} erg s^{-1} (thick lines) and above 10^{40} erg s^{-1} (thin lines) in the average XLF of sources in the nearby galaxies (Mineo et al. 2012) taken in the form (43) as a function of the maximum efficiency. The black solid, blue dotted, red dot–dashed and green dashed curves correspond to models 1–4 from Table 1, respectively.

The pulsar fraction at luminosities in excess of $\log L = 40$ (see Fig. 9b) shows a similar behaviour, but dependence on η_0 is stronger because typically the XLF cuts off at that luminosity even for small initial periods and large σ_p.

The dependence of the pulsar fraction on the maximum efficiency η_0 for the models listed in Table 1 is presented in Fig. 10. Most of the models predict rather flat dependence on η_0 of the pulsar fraction at $\log L > 39$ because of the wide initial period distribution producing the XLF extending to rather high luminosities. The only exception is model 2 (Gonthier et al. 2002), which predicts a significant drop in the pulsar function below $\eta_0 = 0.5$. This is a direct consequence of the fact that this model has a narrow period distribution and its XLF has a sharp cutoff at about $\log L = 39.3$ for $\eta_0 = 1.0$. Thus, we see that for a rather wide range of η_0 between 0.3 and 1 the pulsar fraction above $\log L = 39$ is between about 10 and 30 per cent for all models. Obviously, the beaming can reduce this fraction proportionally and for $b = 0.3$ it is then at least 3 per cent.

For models 1 and 3, the pulsar fraction is even larger at very high luminosities in excess of $\log L = 40$ reaching $0.4b$ and $0.3b$, respectively. In those cases, the dependence on η_0 is also not strong. While for model 2, the pulsar fraction is below 3 per cent and scales approximately as η_0^2. From Fig. 8 it is clear that the closer parameters of the birth periods are to the limiting (bold red) line, the larger is the pulsar fraction. For large σ_p, the cumulative XLF is less steep than the observed XLF and therefore the pulsar fraction is a monotonically growing function that can reach 100 per cent above $\log L = 40$. Thus, it is possible that the pulsar fraction among the brightest ULX is significantly larger than 10 per cent.

4.3 Distribution functions of the luminous pulsars

In order to describe the possible observational appearance of the pulsars that can be observed as ULXs, we find a posteriori distribution of pulsars with luminosities $\log L > 39$ and 40 over magnetic field and birth periods as well as over their true ages. Because the
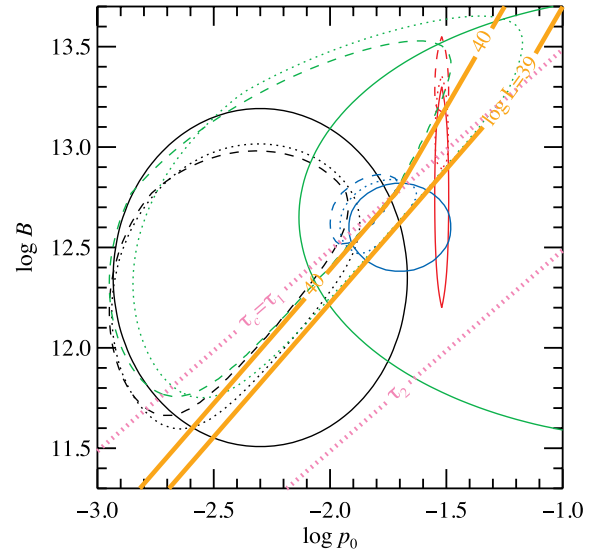

Figure 11. Distribution of pulsars over magnetic field and initial periods. The black, red, green and blue solid curves encircle 90 per cent of pulsars for models 1–4 from Table 1, respectively. The dotted and dashed curves encircle 90 per cent of initial pulsar distribution that can be observed to radiate above 10^{39} erg s^{-1} and 10^{40} erg s^{-1}, respectively. The mean and the standard deviation describing these distributions are given in Table 4. The dotted pink curves give the dependence $\tau_c = \tau_1$ and $\tau_c = \tau_2$. The solid brown curves are the lines of constant X-ray luminosity of 10^{39} and 10^{40} erg s^{-1} for $\eta_0 = 1$.

pulsar luminosity drops with time, we are interested only in pulsars that emit above a given limiting L at birth. On the $\log B$–$\log p_0$ plane, these are the pulsars to the left of the corresponding $L =$ const line (see Figs 1 and 11). The probability that a pulsar will be observed above a given luminosity threshold is proportional to the pulsar age when it crosses the limiting $L =$ const line. Thus, the density distribution of such pulsars on the $\log B$–$\log p_0$ plane (limited to the region left of the limiting luminosity line) is given by the product of the density distribution at birth and the true age $t = (p_c^2 - p_0^2)/\alpha B^2$:

$$P(\log p_0, \log B) \propto t \times H(p_c - p_0) \times G(\log p_0; \log\langle p_0 \rangle, \sigma_p)$$

$$\times G(\log B; \log\langle B \rangle, \sigma_B), \qquad (48)$$

where H is the Heaviside step function and p_c is the pulsar period when it crosses the limiting luminosity line given by equation (10).

These density distributions of the bright observed pulsars for various models from Table 1 are shown in Fig. 11. These distributions are generally narrower than the original distribution and skewed towards smaller periods and larger magnetic fields. They are elongated along the line of constant luminosity. The mean values and the standard deviations of these distributions are given in Table 4. We also find the distribution of true ages of these pulsars, which is a monotonically decreasing function and can be described by the median age τ.

The evolution of the luminosity for the average luminous pulsar can be described as follows: during the first ten years the luminosity is nearly constant at the level of $\sim 10^{40}$ erg s^{-1}. After that it starts to decrease and still exceeds $\sim 10^{39}$ erg s^{-1} for the next 100 yr, during which the pulsars can be observed as ULXs. After that the luminosity decreases down to $\sim 10^{36}$ erg s^{-1} in about 1000 yr.

The rotation-powered pulsars are often assumed to be non-variable sources, but there may exist some variability on the

Table 4. Parameters of the birth period and the magnetic field distributions as well as the median true age of pulsars with observed luminosities in excess of a given value for models from Table 1.

Model	$\log \langle p_0 \rangle$	σ_p	$\log \langle B \rangle$	σ_B	τ yr
		$\log L > 39$			
1	−2.43	0.24	12.35	0.34	343
2	−1.52	0.0	13.13	0.16	96
3	−2.05	0.39	12.79	0.44	136
4	−1.80	0.08	12.67	0.09	105
		$\log L > 40$			
1	−2.46	0.23	12.39	0.32	174
2	−1.52	0.0	13.37	0.13	13
3	−2.22	0.34	12.71	0.41	52
4	−1.86	0.07	12.70	0.08	36

time-scales shorter that ∼100 yr related to the interaction of the SN remnant with the PWN and the surrounding media. As it was shown by Dwarkadas & Gruszko (2012), the SN remnant could show a variability at least on the time-scales ∼10 yr. This variability could depend on the scale and the spatial spectrum of inhomogeneities of the surrounding media, and the characteristic variability time-scale may increase with the pulsar age. The spectrum in the 0.1–10 keV range should consist of the soft thermal component related to the shock and the power-law tail related to the synchrotron radiation both from the shocks and the central pulsar.

5 SUMMARY

In this paper, we have investigated the question whether rotation-powered pulsars and PWN could be observed as some subclass of ULXs, and, if it is so, what is the fraction of pulsars in the whole ULX population.

First, we developed an analytical model of the XLF, by solving the evolution equation for the period distribution of the pulsars. We derived both the steady-state and the time-dependent solution. The steady-state solution is transformed to the pulsar XLF. We showed that this XLF has a broken power-law shape, reflecting the complex behaviour of the efficiency, with the high luminosity cut-off which location and shape are determined by the parameters of the birth period and magnetic field distributions. The location of the cutoff mainly depends on the mean birth period. For short enough birth periods, the cutoff may lie above 10^{39} erg s^{-1}. Therefore, the existence of luminous pulsars is possible.

The time-dependent solution tells us about the evolution of the distribution functions of the pulsars. We have shown that at large ages the period distribution becomes a delta-function-like peaking at $\sqrt{\alpha t}\,B$. The time-dependent luminosity distribution is more complicated due to the complexity of the luminosity–period relation. It can be multimodal with different modes related to the different regimes of the efficiency of conversion of the rotation energy losses to the X-ray radiation. As the age of the pulsars increases, the luminosity distribution becomes more symmetric.

We found constraints on the parameters of the birth period distribution using the observed XLF of the sources in the nearby galaxies obtained by Mineo et al. (2012). We found that the mean birth period cannot be shorter than 10–30 ms, depending on the width of the distribution. Therefore, the parameters derived by Arzoumanian et al. (2002) lie in the forbidden region for the typically assumed pulsar production rates. Accounting for the recent findings of Popov

& Turolla (2012), the parameters obtained by Faucher-Giguère & Kaspi (2006) are the most reliable.

We discussed the influence of the beaming and the maximal efficiency on the luminosity function. For our calculations, we assumed conservatively $b > 0.3$, but the results can be easily scaled to the different values of the beaming. The number of the observed pulsars and their contribution to the ULX population depend linearly on b. The influence of the maximal efficiency is more complex, because it affects only the high luminosity tail of the pulsar XLF. For $\eta_0 = 0.3$ the allowed parameter space of the birth period distribution expands towards the shorter birth periods. The fraction of pulsars in the observed XLF of Mineo et al. (2012) would be smaller for smaller values of the efficiency and it strongly depends on the luminosity above which this fraction is computed. We showed that for broad initial period distributions, the pulsar fraction is a weak function of η_0.

We have also obtained constraints on the period distribution by applying the method proposed by Perna et al. (2008). We derived the luminosity function of core-collapse SNe, using published X-ray light curves and compared it to the time-dependent luminosity function for pulsars. We found that the observed luminosities of the SNe are consistent with the mean birth period of $p_0 \gtrsim 0.015$–1 s, depending on the width of the distribution, maximum efficiency and the beaming factor. These constraints are in agreement with those derived by Perna et al. (2008).

We estimated a possible fraction of the pulsars in the whole population of ULX, using the observed XLF from Mineo et al. (2012). For the models considered in the previous studies of pulsar populations, the predicted fraction of luminous pulsars can be in excess of 3 per cent for the sources with luminosities greater than 10^{39} erg s^{-1}. At this moment, about 500 ULXs have been discovered (Feng & Soria 2011; Swartz et al. 2011; Walton et al. 2011) and we expect that at least ∼15 of those should be associated with the rotation-powered pulsars. The models predict the pulsar fraction above 10^{40} erg s^{-1} at the level of 1–40 per cent.

Therefore, we might potentially observe bright pulsars as ULXs in galaxies with high SFR. These pulsars should have almost constant luminosity during the first hundred years after their birth, but there may exist some variability on the time-scale of ∼10 yr related to the interaction of the expanding SN remnant shell with the surrounding media.

ACKNOWLEDGEMENTS

REFERENCES

Arzoumanian Z., Chernoff D. F., Cordes J. M., 2002, ApJ, 568, 289
Becker W., Truemper J., 1997, A&A, 326, 682
Chevalier R. A., 1989, ApJ, 346, 847
Chevalier R. A., Fransson C., 1994, ApJ, 420, 268
Chomiuk L., Povich M. S., 2011, AJ, 142, 197
Colbert E. J. M., Mushotzky R. F., 1999, ApJ, 519, 89
Dwarkadas V. V., Gruszko J., 2012, MNRAS, 419, 1515
Fabbiano G., 1988, ApJ, 325, 544
Fabbiano G., 1989, ARA&A, 27, 87
Fabbiano G., Trinchieri G., 1987, ApJ, 315, 46
Fabrika S., 2004, Astrophys. Sp. Phys. Rev., 12, 1
Faucher-Giguère C.-A., Kaspi V. M., 2006, ApJ, 643, 332
Feng H., Kaaret P., 2010, ApJ, 712, L169
Feng H., Soria R., 2011, New Astron. Rev., 55, 166

Ghosh P., 2007, Rotation and Accretion Powered Pulsars. World Scientific Press, Singapore, Singapore

Gladstone J. C., Roberts T. P., Done C., 2009, MNRAS, 397, 1836

Gonthier P. L., Ouellette M. S., Berrier J., O'Brien S., Harding A. K., 2002, ApJ, 565, 482

Heger A., Fryer C. L., Woosley S. E., Langer N., Hartmann D. H., 2003, ApJ, 591, 288

Immler S., Pooley D., 2007, Astron. Telegram, 1004

Immler S., Brown P. J., Filippenko A. V., Pooley D., 2007, Astron. Telegram, 1290

Immler S., Pooley D., Brown P. J., Milne P., 2009, Astron. Telegram, 1918

Kaaret P., Corbel S., Prestwich A. H., Zezas A., 2003, Sci, 299, 365

Kaaret P., Alonso-Herrero A., Gallagher J. S., Fabbiano G., Zezas A., Rieke M. J., 2004, MNRAS, 348, L28

Kajava J. J. E., Poutanen J., 2009, MNRAS, 398, 1450

Kargaltsev O., Pavlov G. G., 2008, in Bassa C., Wang Z., Cumming A., Kaspi V. M., eds, Proc. AIP Conf. Ser. Vol. 983, 40 Years of Pulsars: Millisecond Pulsars, Magnetars and More. Am. Inst. Phys., New York, p. 171

King A. R., Davies M. B., Ward M. J., Fabbiano G., Elvis M., 2001, ApJ, 552, L109

Long K. S., van Speybroeck L. P., 1983, in Lewin W. H. G., van den Heuvel E. P. J., eds, Accretion-driven Stellar X-ray Sources. Cambridge Univ. Press, Cambridge, p. 117

Miller J. M., Fabbiano G., Miller M. C., Fabian A. C., 2003, ApJ, 585, L37

Mineo S., Gilfanov M., Sunyaev R., 2012, MNRAS, 419, 2095

Perna R., Stella L., 2004, ApJ, 615, 222

Perna R., Soria R., Pooley D., Stella L., 2008, MNRAS, 384, 1638

Popov S. B., Turolla R., 2012, Ap&SS, 341, 457

Possenti A., Cerutti R., Colpi M., Mereghetti S., 2002, A&A, 387, 993

Poutanen J., Lipunova G., Fabrika S., Butkevich A. G., Abolmasov P., 2007, MNRAS, 377, 1187

Poutanen J., Fabrika S., Valeev A. F., Sholukhova O., Greiner J., 2012, MNRAS, preprint (arXiv:1210.1210)

Ptak A., Colbert E., van der Marel R. P., Roye E., Heckman T., Towne B., 2006, ApJS, 166, 154

Servillat M., Farrell S. A., Lin D., Godet O., Barret D., Webb N. A., 2011, ApJ, 743, 6

Seward F. D., Wang Z.-R., 1988, ApJ, 332, 199

Stocke J. T., Morris S. L., Gioia I. M., Maccacaro T., Schild R., Wolter A., Fleming T. A., Henry J. P., 1991, ApJS, 76, 813

Swartz D. A., Tennant A. F., Soria R., 2009, ApJ, 703, 159

Swartz D. A., Soria R., Tennant A. F., Yukita M., 2011, ApJ, 741, 49

Takata J., Wang Y., Cheng K. S., 2011, MNRAS, 415, 1827

Tauris T. M., Manchester R. N., 1998, MNRAS, 298, 625

Vink J., Bamba A., Yamazaki R., 2011, ApJ, 727, 131

Walton D. J., Roberts T. P., Mateos S., Heard V., 2011, MNRAS, 416, 1844

Zezas A., Fabbiano G., Rots A. H., Murray S. S., 2002, ApJ, 577, 710

This paper has been typeset from a TEX/LATEX file prepared by the author.